# General Disclaimer

One or more of the Following Statements may affect this Document

- This document has been reproduced from the best copy furnished by the organizational source. It is being released in the interest of making available as much information as possible.

- This document may contain data, which exceeds the sheet parameters. It was furnished in this condition by the organizational source and is the best copy available.

- This document may contain tone-on-tone or color graphs, charts and/or pictures, which have been reproduced in black and white.

- This document is paginated as submitted by the original source.

- Portions of this document are not fully legible due to the historical nature of some of the material. However, it is the best reproduction available from the original submission.

APL/JHU
S1R78U-009
FEBRUARY 1977
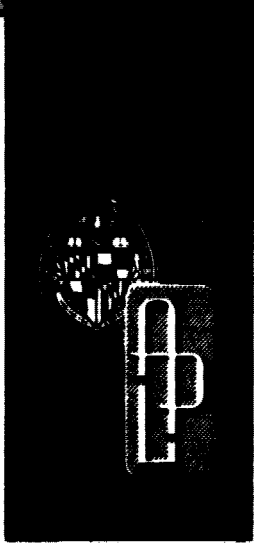
PREDICTION OF ATTENUATION OF THE 28 GHz COMSTAR BEACON SIGNAL USING RADAR AND MEASURED RAIN DROP SPECTRA

by JULIUS GOLDHIRSH
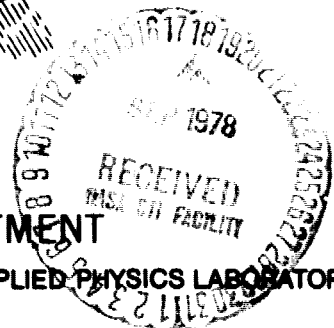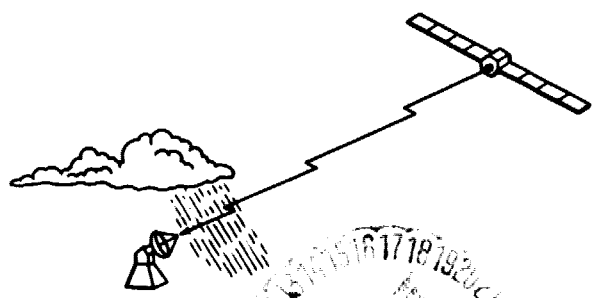
SPACE DEPARTMENT

THE JOHNS HOPKINS UNIVERSITY ■ APPLIED PHYSICS LABORATORY

PREDICTION OF ATTENUATION OF THE 28 GHz COMSTAR BEACON SIGNAL USING RADAR AND MEASURED RAIN DROP SPECTRA

by JULIUS GOLDHIRSH

TABLE OF CONTENTS

LIST OF FIGURES

LIST OF FIGURES (continued)

iv

LIST OF TABLES

PREDICTION OF ATTENUATION OF THE 28 GHz COMSTAR BEACON SIGNAL
USING RADAR AND MEASURED RAIN DROP SPECTRA

Abstract

A program to measure the rain attenuation of the COMSTAR beacon signal at 28.56 GHz has been in continuous operation since March of 1977 at Wallops Island, Virginia. During the summer of 1977, simultaneous radar and disdrometer measurements were also made and used for predicting path attenuation. The best fit values of a and b of the relation $k = a Z^b$ were deduced for each rain period from the raindrop size measurements; where k is the attenuation coefficient [dB/km] and Z is the relfectivity factor $[mm^6/m^3]$. The measured k-Z relations and the simultaneous radar reflectivity measurements along the beacon path were injected into a computer program for estimating the path attenuation. Predicted attenuations when compared with the directly measured ones showed generally good correlation on a case by case basis and very good agreement statistically.

The results demonstrate the utility of using radar in conjunction with disdrometer measurements for predicting fade events and long term fade distributions associated with earth-satellite telecommunications. It also suggests its use for arriving at sampled fade distributions from which prediction criteria associated with variable path angle, frequency, and site diversity can be tested.

PREDICTION OF ATTENUATION OF THE 28 GHz COMSTAR BEACON SIGNAL
USING RADAR AND MEASURED RAIN DROP SPECTRA

1.0   INTRODUCTION

The ability to use radar as a predictor of rain attenuation has
been previously tested against actual direct measurements by several
investigators. McCormick [1] and Strickland [2] correlated their 3 GHz
radar data with path attenuations at 15.3 GHz; the former investigator
using a beacon on an aircraft, and the latter using transmissions from the
ATS-5 satellite. Goldhirsh [3] correlated his 3 GHz radar measurements
with 13 and 18 GHz measured attenuations using the ATS-6 in an uplink mode.
Although some statistical aspects were considered by the above investiga-
tors, none examined how well cumulative fade distributions as derived from
radar compared with those obtained from direct measurements. More recently,
Hodge and Austin [4] compared radar measurements at 3 GHz using the McGill
radar with radiometer-predicted attenuation at 13 GHz and were able to
arrive at predictive parameters as well as a radar calibration by matching
radar and radiometer-derived cumulative fade distributions.

We describe here an experiment performed at Wallops Island, Va.,
using a disdrometer and radar system for estimating the rain attenuation
of the COMSTAR beacon signal at 28.56 GHz. Drop size distributions
measured during each rain period enabled the calculation to be made of
empirical parameters which were injected into the radar prediction scheme.
In this way, the dominant drop size distribution for each rain period was
used. Results using the measured drop size spectra are compared with those
using the Marshall-Palmer distribution [5]. Individual case histories and
overall cumulative fade distribution comparisons are presented. The data
base corresponds to five rain days during the summer of 1977 (June through
September) and represents 13 attenuation events and 304 minutes of simul-
taneous radar data.

2.0   EXPERIMENTAL CONFIGURATION

2.1   General

The experimental configuration which is depicted in Fig. 1 con-
sists of a phase locked loop receiving system operating at 28.56 GHz, an

S-band radar (f = 2.84 GHz) located approximately 30 m away, and a system
of three raingages and two disdrometers for measuring rain drop size
distributions located in the immediate vicinity of the receiving antenna.
Both antennas are fixed and point in the direction of the COMSTAR
geosynchronous satellite [95°W longitude ± 0.1°] with elevation and azimuth
angles of 41.6° and 210°, respectively.

In Fig. 2 are shown the geographical location of Wallops Island
(WI), Va., and the azimuth pointing direction. The circled region about
WI represents the radar observation area.

The satellite receiver as well as the disdrometer-raingage system
are functioning continuously for arriving at long term statistics (to be
described in a future report). During selected periods of rain, the radar
monitors the reflectivity along a parallel path for purposes of testing
radar methods for predicting the path attenuation at 28.56 GHz. The dis-
drometer data are used as input in these prediction methods.

2.2 Receiver System

The pertinent parameters for the COMSTAR receiving system are
given in Table 1. The system (Fig. 3) consists of an rf front end mounted
at the antenna location. The IF output of 1.05 GHz feeds a phase lock loop
receiver located in the radar building. The output voltage ranges from
0 to 5 VDC and covers the input dynamic range of 32 dB. This output is
continuously recorded on a calibration strip chart. In addition, the out-
put signal is coded and recorded on one channel of a four channel tape
recorder. The tape recorder is automatically actuated whenever the attenu-
ation exceeds a defined threshold, a raingage bucket tip occurs, or a drop
impacts on the disdrometer sensors.

Calibration of the receiver system (Fig. 4) is performed by in-
jecting a stable 1.05 GHz signal at various levels into the front end where
it is upconverted and routed (switch in up position) through the mixer pre-
amplifier downconverter. The 1.05 GHz IF output passes through the phase
locked loop system. Calibrations are performed daily and recorded on tape.
On several occasions, the satellite beacon signal was used as a source with

SATELLITE LONG.	WI RECEIVER	
	AZ	EL
128° W	244.8°	20.6°
95° W	210.0°	41.0°

COMSTAR SATELLITE BEACON SIGNAL
f = 28.56 GHz

150 m

BW = 0.4°

BW = 0.4°

θ_o

θ_o

D = 18.3 m

D = 1.8 m

SPANDAR S-BAND RADAR
f = 2.84 GHz

COMSTAR RECEIVER
f = 28.56 GHz

DISDROMETER RAINGAGE SYSTEM
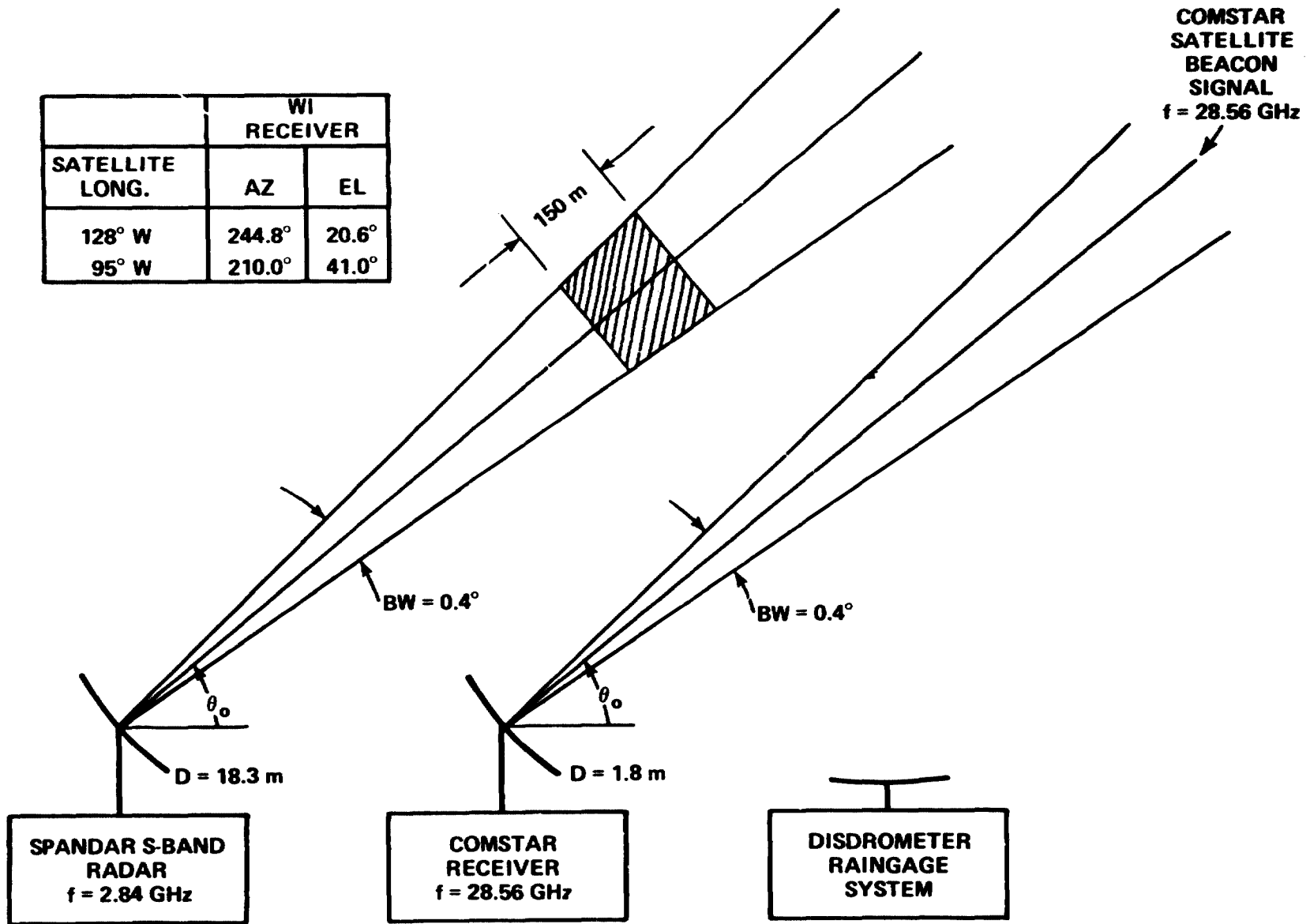
Figure 1. Experimental configuration at Wallops Island, Virginia. Antennas point in the direction of the Satellite at 95°W longitude.
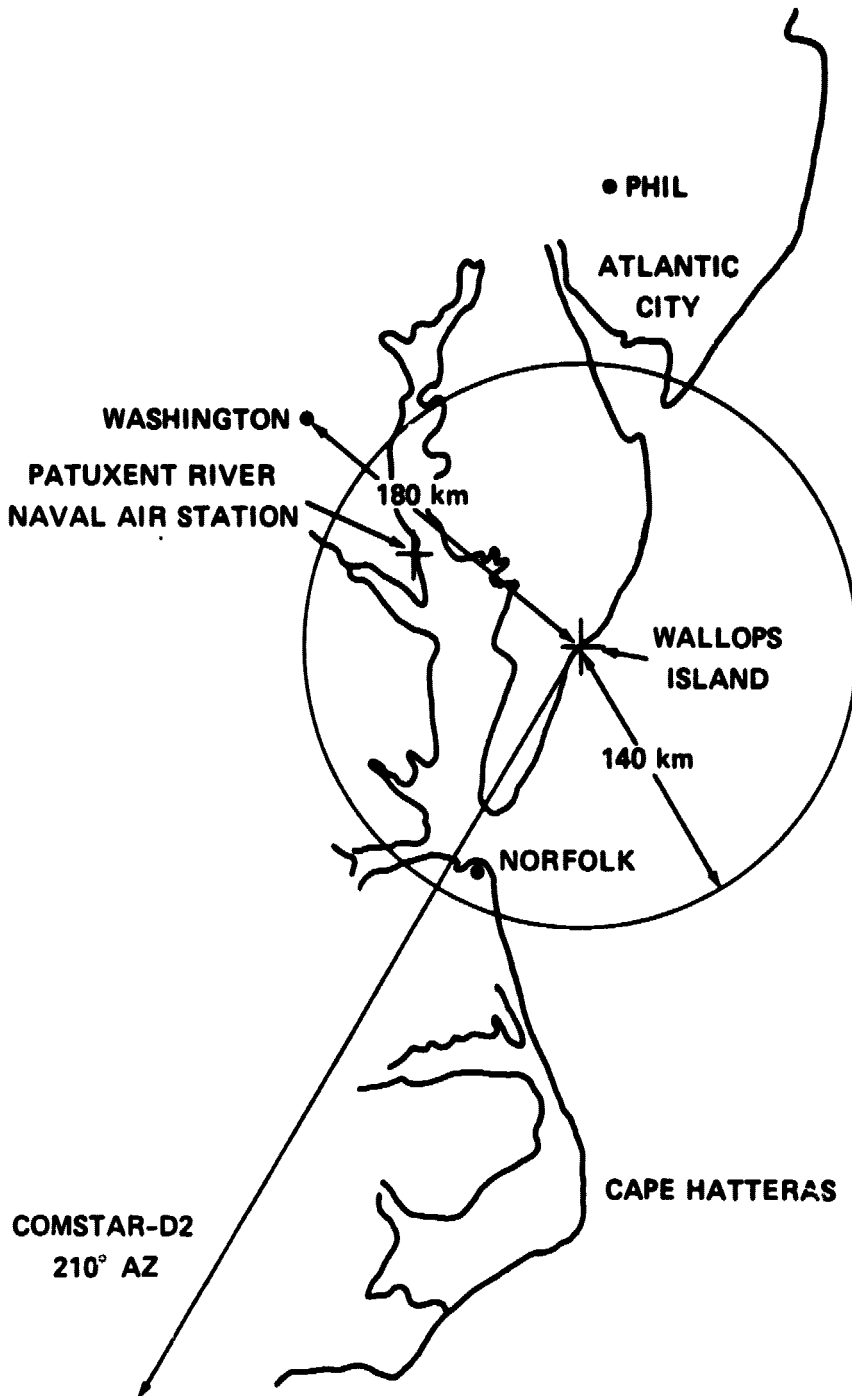
Figure 2. Geographic location of test site.

Table 1

PERTINENT COMSTAR RECEIVING SYSTEM PARAMETERS

Antenna Gain	52.7 dB
Beamwidth	0.4°
Antenna Diameter	1.83 m (6 ft)
Free Space Power Received	-106 dBm
ERP	55.8 dBm
Path Loss	-213.4 dB
Line Loss	-0.5 dB
Sky Loss	-0.3 dB
Phaselock Hold-In Threshold	-138 dBm
Phaselock Acquisition Threshold	-133 dBm
Dynamic Range (Minimum)	32 dB
Predetection 3 dB Bandwidth	50-100 Hz
Post Detection 1 dB Bandwidth	10-20 Hz
Amplitude Measurement Error	$\pm$ 1 dB
Noise Figure	18 dB
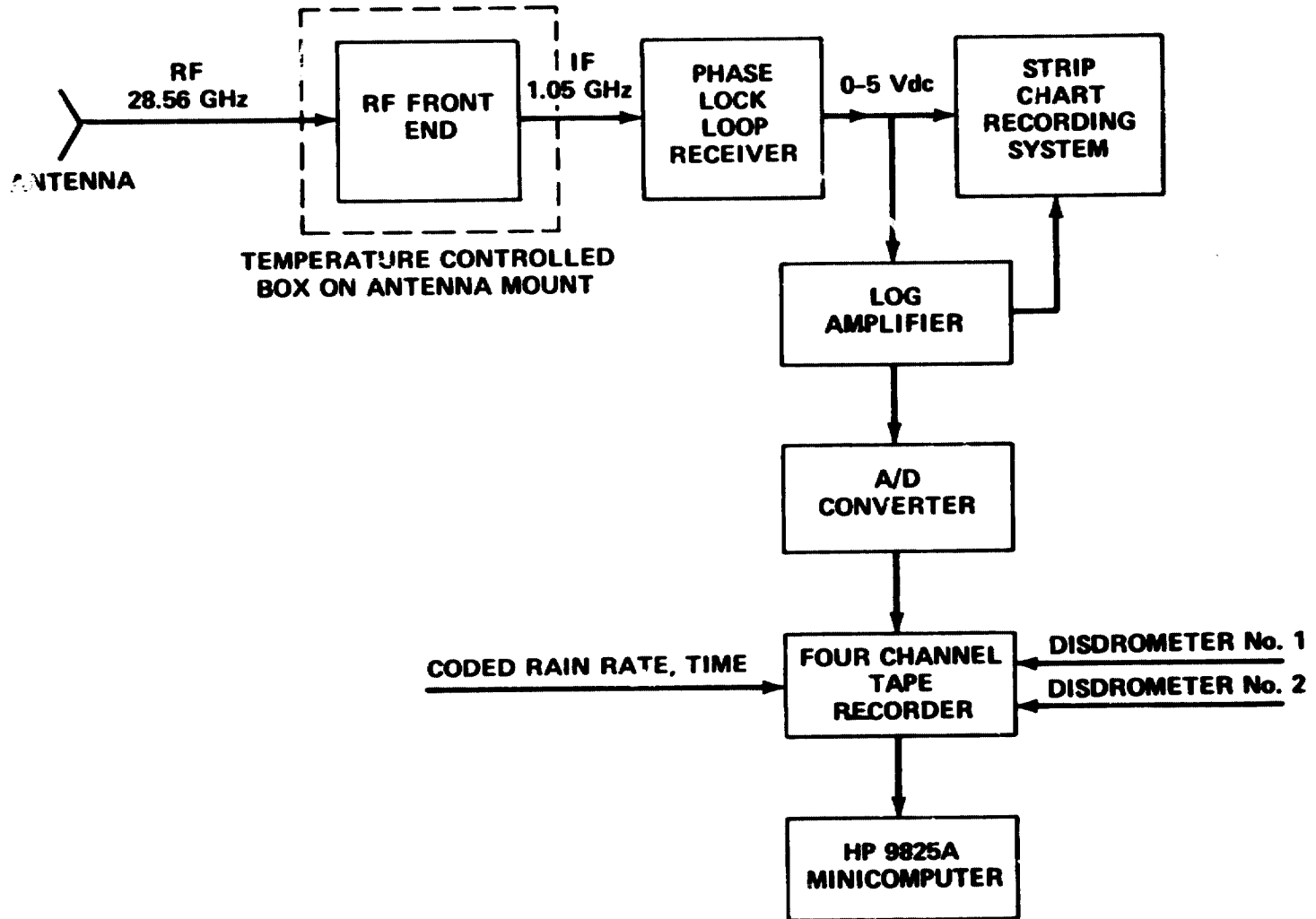
Figure 3. Elements of satellite receiving configuration.

L. O.
f = 27.51

IMAGE
FILTER

f = 28.56

1.05 GHz
TEST SIGNAL

MIXER
(UPCONVERTER)

CALIBRATION
LOOP

RECEIVER
SIGNAL IN
f = 28.56 GHz

IMAGE
FILTER

1.05 GHz
OUT

MIXER-PREAMP
(DOWNCONVERTER)

L. O.
f = 27.51
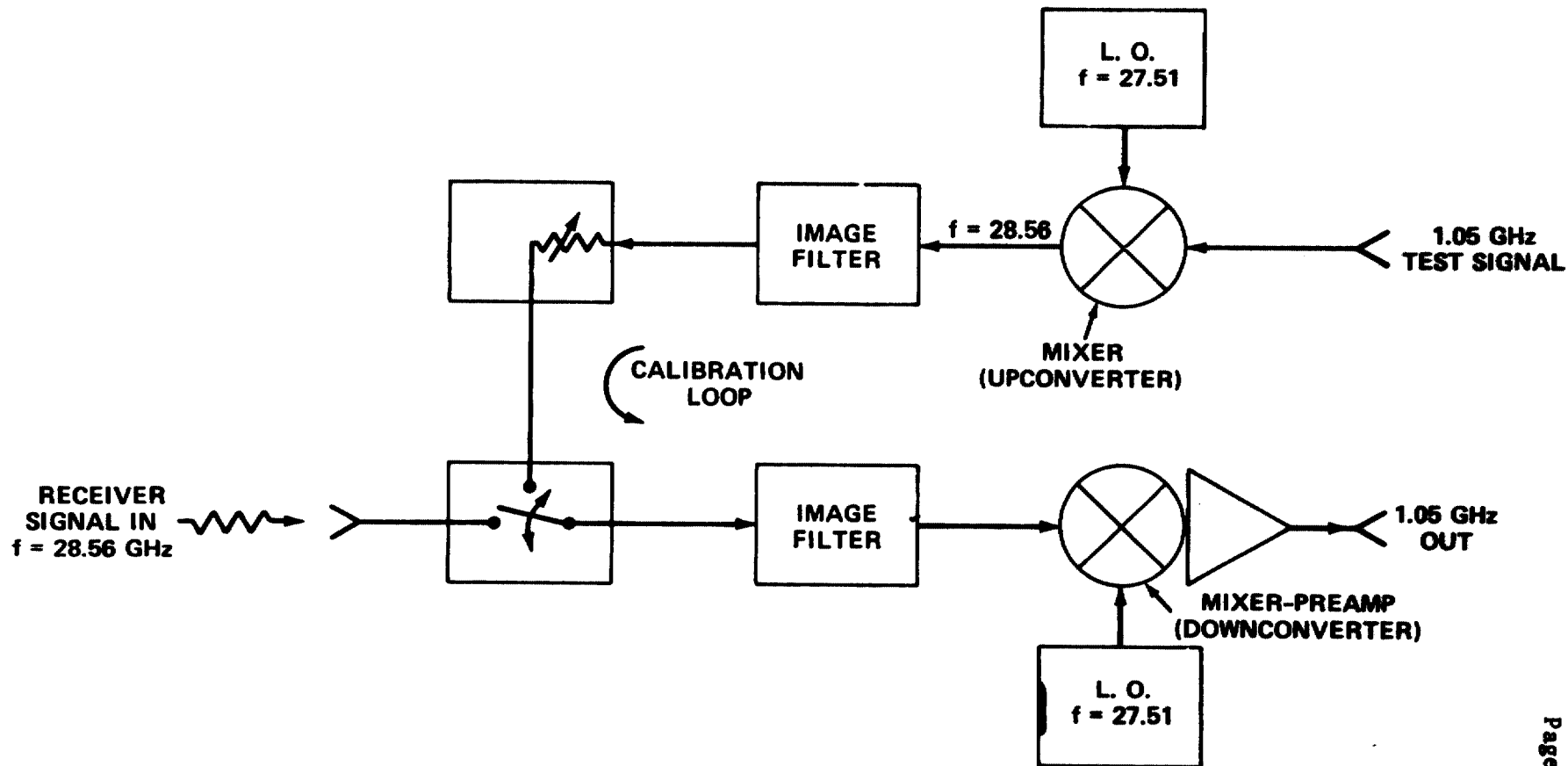
Figure 4.   Calibration configuration for the COMSTAR receiver.

the attenuation placed at the rf front end input. These latter calibra-
tions are within ± 0.5 dB of the loop calibrations.

Since the satellite position is maintained fixed through
stationkeeping to within ± 0.1°, the receiver antenna is also kept fixed.
However, an approximate weekly adjustment of the antenna pointing is made
whenever the satellite assumes a new nodal position. The motion of the
satellite within its ± 0.1° spatial box results in a free space diurnal
variation of less than 2 dB which is p:. dictable to within ± 0.5 dB.

The reflection losses due to water on the feed were measured by
controlled water spray tests and were observed to be on the average of 2 dB
within an uncertainty of ± 1 dB using a hydrophobic agent (Fusidox M)*.

2.3 Radar System

The operating parameters of the radar (SPANDAR) are listed in
Table 2.

During selected periods of rain, the radar reflectivity is
monitored at adjacent range bins along the path where each bin has resolu-
tion of 150 m (1 µsec pulsewidth). The resulting reflectivity represents
the average of 128 independent samples obtained in 0.4 seconds (prf - 320
Hz) using a frequency diversity transmission scheme where each pulse in the
prf is shifted by an amount greater than the inverse pulsewidth [6]. The
integrated data are stored on IBM compatible tape for later analysis on the
IBM 360/91 computer.

The electrical parameters of the radar have been directly cali-
brated [7] and are routinely checked by tracking 6-inch spheres on ballons
[8] and by monitoring the solar flux from the sum at 2.84 GHz [9]. Rela-
tive standard gain horn measurements are also periodically performed. The
accuracy of the absolute calibration of SPANDAR based on on-going measure-
ments as well as previous component calibrations [7] is well within ± 1.5
dB.

*
Silibond Product, Inc., 25 Industrial Way, Wilmington, Massachusetts
01887

Table 2

OPERATING PARAMETERS OF SPANDAR

Radar	FPS/18
Gain	50.6 dB
Peak Power	1.0 MW
Beamwidth	0.4°
Diameter	18.3 m (60 ft)
Frequency Diversity:	
Center Frequency	2.840 GHz
Frequency Excursion, Δf	$\pm$ 13.5 MHz
Pulse Length	1 µsec
Pulse Range Resolution	150 m
prf	320 pps
Number of Pulses Integrated	128
Averaging Time	0.4 sec
Number of Adjacent Range Gates	871
Calibration Error (rms)	< 2 dB

2.4 Disdrometer-Raingage System

The raingages used are of the tipping bucket variety and the disdrometers which were developed at APL [10,11] are of the impact type. In Fig. 5 is shown a cross section view of the sensor itself. When a drop impacts at terminal velocity on the plexiglass aperture, a voltage is induced at the piezoelectric transducer and this voltage is proportional to the drop momentum. The transducer output voltage is passed through a pre-amplifier, shaping circuitry, a biphase encoder, and ultimately to one channel of the four channel tape recorder. Calibrations of the disdrometers are performed by dropping drops of known diameters through capillaries at sufficient heights so that drop terminal velocities are achieved.

The basic elements of the disdrometer-raingage system are given in the block diagram in Fig. 6. The coded outputs of two disdrometers are each fed into one channel of a four channel tape recorder. Outputs of three raingages are multiplexed with a time code (IRIG B Clock) and fed into another channel of the tape recorder. Simultaneously the raingage and disdrometer rain rates obtained using hard wire circuitry are recorded side by side on a chart recording system. A real time comparison of these rain rates represents an on-going check on the performance of the disdrometer.

3.0 ANALYTICAL ASPECTS

3.1 Radar Near Field Correction

Since reflectivities are measured at ranges as close as 600 m away from SPANDAR, and the far zone distance, r_f, is

$$r_f = \frac{2D^2}{\lambda} = 6.3 \text{ km} \tag{3.1}$$

it is necessary to account for near zone effects. In this section we describe a method which enabled the measurement of reflectivities to be made as close in as 600 m by correcting the range-dependent gain and beamwidth in the near field region.

For a tapered aperture illumination, the gain reduces and the beamwidth increases for axial distances smaller than r_f. At the shorter

Piezoelectric
transducer

Output connectors

Plexiglass

Brass tubing

Rubber "O" rings

Scale 1"

Brass

Gasket

Piezoelectric
transducer
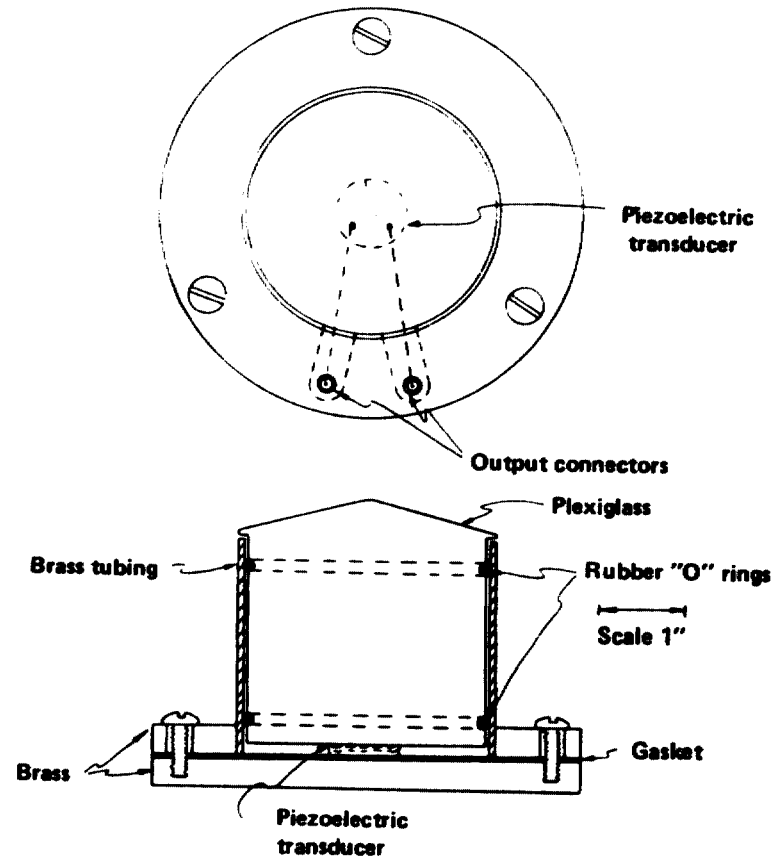
Figure 5.   Cross sectional view of the disdrometer sensor.
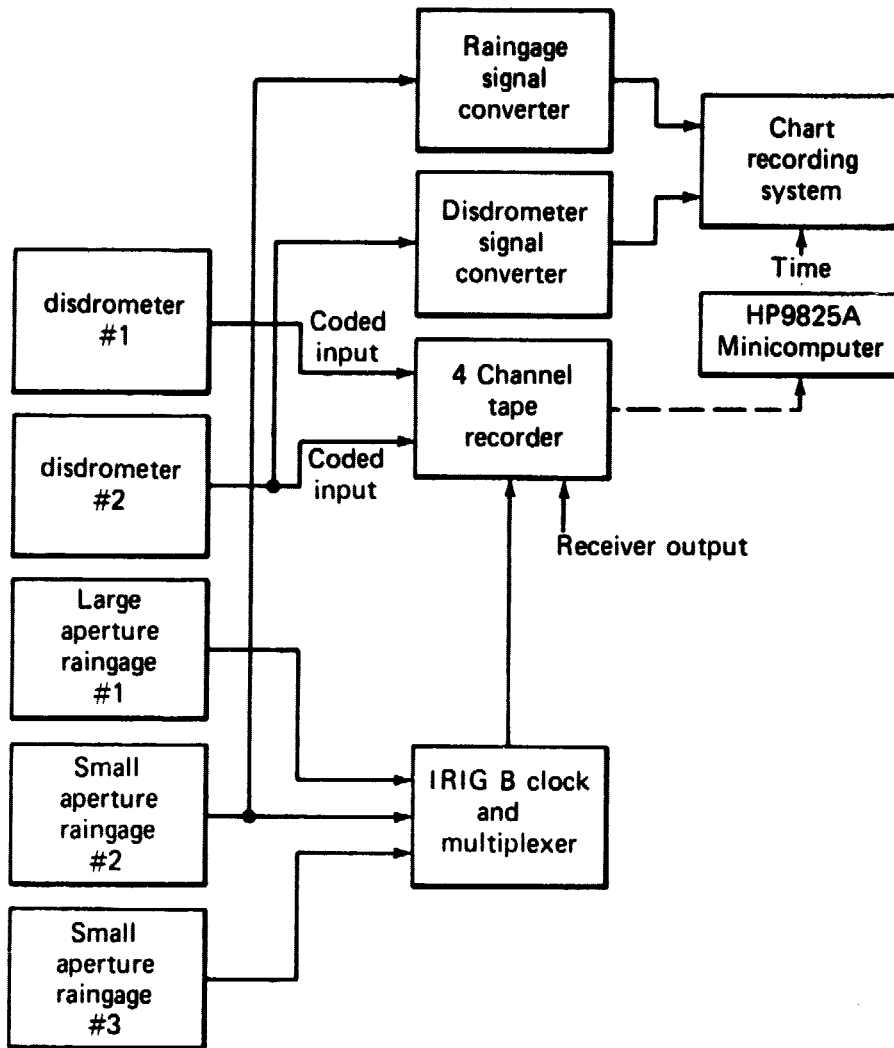
Figure 6.   Basic elements of disdrometer-raingage system.

ranges there results a monotonic increase in power density (at a rate smaller than $1/r^2$) down to $0.1 \, (2D^2/\lambda)$. At closer ranges oscillations occur with a diminishing envelope [12].

It is apparent from the above that the radar equation must be appropriately modified so as to account for the near field effects. In Appendix A we have modified the radar equation using the near field formulation of Hansen [12] to be applicable down to $0.1 \, (2D^2/\lambda) \simeq 600$ m. At closer ranges the clutter of SPANDAR does not allow any further adjustment and we therefore assume the reflectivity to be uniform for the first 600 m of range and use the value measured at 600 m. Using the results of Appendix A, the near zone power, $P(r)$, is obtained by dividing the far zone power formulation, $P_o(r)$, by the appropriate range dependent correction factor, $C(r)$. That is,

$$P(r) = \frac{P_o(r)}{C(r)} \tag{3.2}$$

where,

$$[C(r)]^{-1} = \left(\frac{r}{r_f}\right)^2 \beta(r) \tag{3.3}$$

and where,

$$r \leq r_f = \frac{2D^2}{\lambda} \tag{3.4}$$

$$\beta(r) = \frac{256}{\pi^2} \left\{ 1 - \frac{16X}{\pi} \sin\left(\frac{\pi}{8X}\right) + \frac{128}{\pi^2} X^2 \left[1 - \cos\left(\frac{\pi}{8X}\right) \right] \right\} \tag{3.5}$$

$$X = \frac{r}{r_f} \tag{3.6}$$

The reflectivity factor in the near zone, Z [dBZ] is related to the reflectivity factor using the far zone formulation by the relation,

$$Z[dBZ] = Z_0[dBZ] + 10 \, Log_{10} \, C(r) \tag{3.7}$$

The correction factor C(r) may be shown to be the ratio of the far field gain to the near field gain. That is,

$$C(r)_{dB} = 10 \, Log_{10} \left\{ \frac{G_0}{G(r)} \right\} \tag{3.8}$$

In Fig. 7, $C(r)_{dB}$ is plotted as a function of range from SPANDAR. We may deduce from this curve, for example, that at 0.1 $(2D^2/\lambda)$ = 600 m from SPANDAR, a correction of 4.3 dB must be added to the reflectivity factor calculated using the far zone formulation. The correction factor given by (3.3) was used in the radar program to arrive at the corrected reflectivity factors in the near region as described above.

3.2 Radar Prediction Formulation

We here describe the formulations used in arriving at the radar and disdrometer predicted attenuations and subsequent probability levels.

The radar power recorded in each of the adjacent range bins is converted into reflectivity factor levels, Z $[mm^6/m^3]$ and these are injected in the formulation for path attenuation given by,

$$A_R(t) = \sum_{i=1}^{N} k_i \, \Delta r \qquad [dB] \tag{3.9}$$

where

$$k_i = a \, Z_i^{\,b} \qquad [dB/km] \tag{3.10}$$
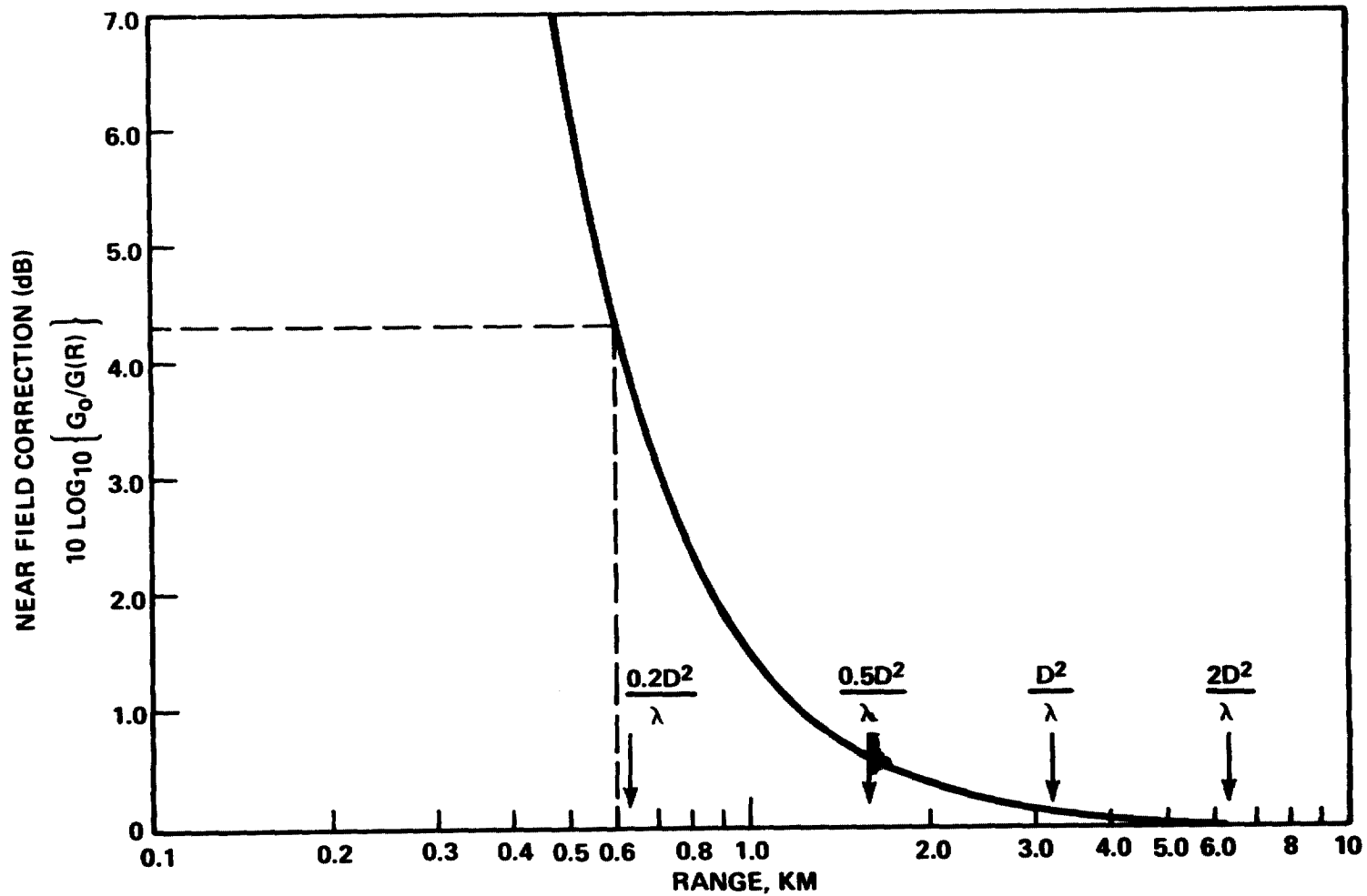
Figure 7. Near field correction factor as a function of range from SPANDAR.

and where

$A_R(t)$ = the radar predicted attenuation in time, t [dB]

r_i = the attenuation coefficient pertaining to i^{th} range bin [dB/km]

$Z(r_i)$ = the reflectivity factor at i^{th} range bin [mm^6/m^3]

Δr = range resolution interval (150 m)

N = number of range bins used in summation (see text)

The limit, N, in (3.9) is obtained in the following way. Through the observation of photographs of RHI's taken at 1/2 hour to 1 hour intervals, it is noted as to whether the rains are either convective or non-convective; the latter showing a bright band and the former showing cellular activity rising to elevations above the zero degree isotherm height. The summation is taken up to a range corresponding to a zero degree isotherm height when a bright band appears since the dominant presence of ice above this height causes negligible attenuation. On the other hand, the summation is taken along the entire path when the rain is convective; implying the dominant presence of water above the zero degree isotherm height. This procedure has been found to give good results both in the previous work [3] as well as in the present experiment.

The values of a and b were arrived at by sampling continuous 30 second drop size distributions (hereafter referred to as DSD) with the APL disdrometer during each rain period and calculating

$$k = \int_{D_{min}}^{D_{max}} N(D) \, C_{ext}(D) \, dD \qquad [dB/km] \qquad (3.11)$$

$$Z = \int_{D_{min}}^{D_{max}} N(D) \, D^6 \, dD \qquad [mm^6/m^3] \qquad (3.12)$$

where

k = theoretical attenuation coefficient [dB/km]

$N(D)dD$ = number of drops per unit volume between drop sizes D and D+dD (DSD)

$C_{ext}(D)$ = extinction factor (dB/km) x cm^3

Z = theoretical reflectivity factor $[mm^6/m^3]$

D_{min}, D_{max} = the minimum and maximum diameter measured, respectively.

Best fit values of a and b were generated for each rain period; the rain period representing a continuous rain event for the day in question. The extinction factors for 28.56 GHz, $C_{ext}(D)$, were arrived at by interpolating the results of Medhurst [13].

4.0 RESULTS

As mentioned previously, the results presented here correspond to the summer of 1977 during which approximately five hours of radar data of rain were obtained simultaneous with path attenuation measurements. This period encompassed five rain days and 13 attenuation events. The disdrometer results presented were taken from data acquired over a period which flanked the radar measurements.

In Table 3 are summarized the sampling days and times for both the radar and disdrometer measurements. Also listed are the measured best fit parameters a and b (5th and 6th columns) pertaining to the relation (3.10) for the indicated rain events. In the 7th column are given values of the coefficient of correlation, r^2, which establishes a measure of the goodness of fit; 1 being perfect. In establishing the number of samples and to ensure a statistically adequate drop size number, only those spectra were selected in which the rain rate exceeded 2.5 mm/hr.

4.1 Empirical Relations from Drop Size Spectra

Examples showing scatter plots of log k versus log Z are given in Figs. 8 through 11 for days 157 (June 6), 236 (August 24, afternoon and evening rain periods), and 257 (September 14). Each point is representative

Table 3

SUMMARY OF SAMPLING DAYS AND TIMES AND CORRESPONDING DISDROMETER RESULTS

Date (Julian Day) 1977	Event No.	Sampling Time Intervals		Disdrometer Best Fit Parameters			
		Radar	Disdrometer	a	b	r^2	No. of Samples
June 6 (157)	1	21:26-21:55	21:26-22:45	1.17×10^{-3}	0.825	0.93	123
	2	21:57-22:26					
	3	22:36-22:48					
June 9 (160)	4	12:44-13:13	12:44-14:49	7.36×10^{-3}	0.617	0.75	180
	5	13:24-13:53					
	6	14:41-14:50					
Aug 24 (236)	7	14:56-15:24	14:20-16:30	1.23×10^{-2}	0.492	0.60	102
	8	15:38-16:07					
	9	16:09-16:25					
Aug 24-25 (236-237)	10	23:35-23:59	23:30-00:52	1.45×10^{-3}	0.806	0.94	107
	11	00:05-00:34					
Sept 14 (257)	12	20:03-20:32	20:03-20:46	3.47×10^{-3}	0.733	0.95	53
	13	20:33-20:48					
Overall Data Base		304 min	458 min	1.87×10^{-3}	0.775	0.89	565
Marshall-Palmer				2.01×10^{-3}	0.773		

of a 30-second drop size distribution where the corresponding calculations
are made using (3.11) and (3.12). The solid line shown in each of the
figures represent the best fit linear regression line used for that rain
period.

In Fig. 12 are shown the best-fit k-Z curves plotted side by side
for the five rain days. Also shown is the Marshall-Palmer (hereafter
referred to as M-P) best-fit curve. We note that the distributions for three
of the five rain periods (June 6, August 24-25, and September 14) are close
to the M-P line. It may be noted that when all the drop size distributions
are considered together, the values of a and b (Table 1) are almost identical
with those corresponding to the M-P distribution (i.e., a = 2.10×10^{-3},
b = 0.773). This is attributed to the fact the M-P distribution is repre-
sentative of a large data base for the geographic region of Washington, D. C.
(mid-Atlantic east coast). On an individual rain period basis the values of
a and b may be markedly different from the M-P distribution as is indicated
for the June 9 and August 24 periods.

Other interesting features of the above results are that the drop
size distributions for two distinct rain periods occurring for the same day
may be markedly different as evidenced by the results of August 24. It also
may be noted from Table 1 that the smaller the coefficient of correlation,
the greater the deviation from the M-P, and where r^2 exceeds 0.9, the fit
is close to M-P.

4.2 Measured and Predicted Attenuation Events

In Figs. 13 through 17 are given examples of attenuation versus
time plots of the predicted and measured attenuations corresponding to the
best-fit regression parameters a and b obtained from the scatter plots of
Figs. 8 through 11. The ordinate and abscissa in each of these curves
represent the attenuation in dB and time in GMT, respectively. The solid
curve represents the measured level, the dashed curve the predicted level
using (3.9) and the measured empirical parameters, a and b. Also plotted
is a dot-dashed curve which represents the attenuation obtained using (3.9)
and a and b corresponding to the M-P distribution. The directly measured
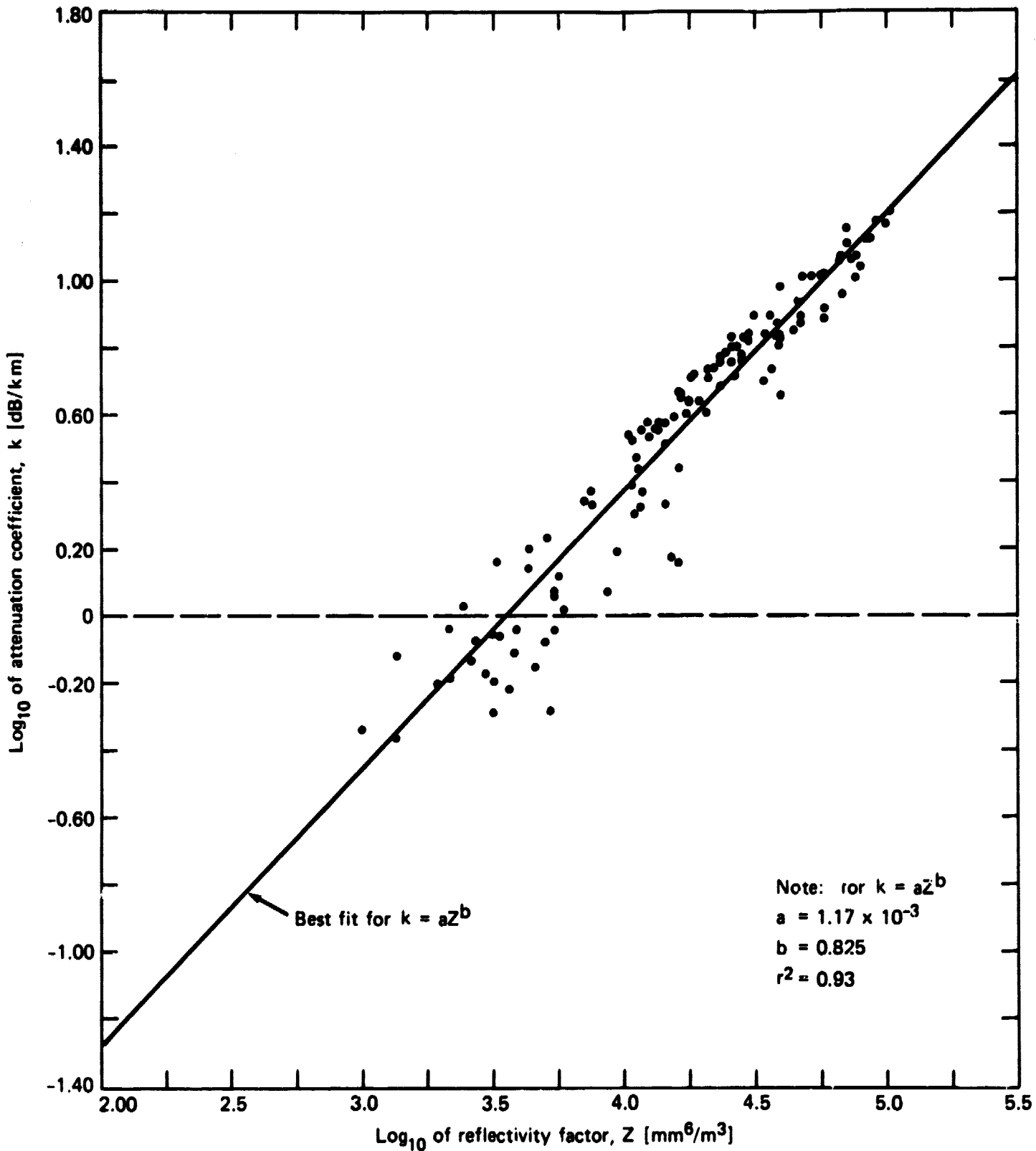
Figure 8. Scatter plot of log k vs log Z for June 6, 1977 (day 157)
from 21 hr, 26 min to 22 hr, 45 min GMT. Solid line is
best fit for $k = a Z^b$ relation.
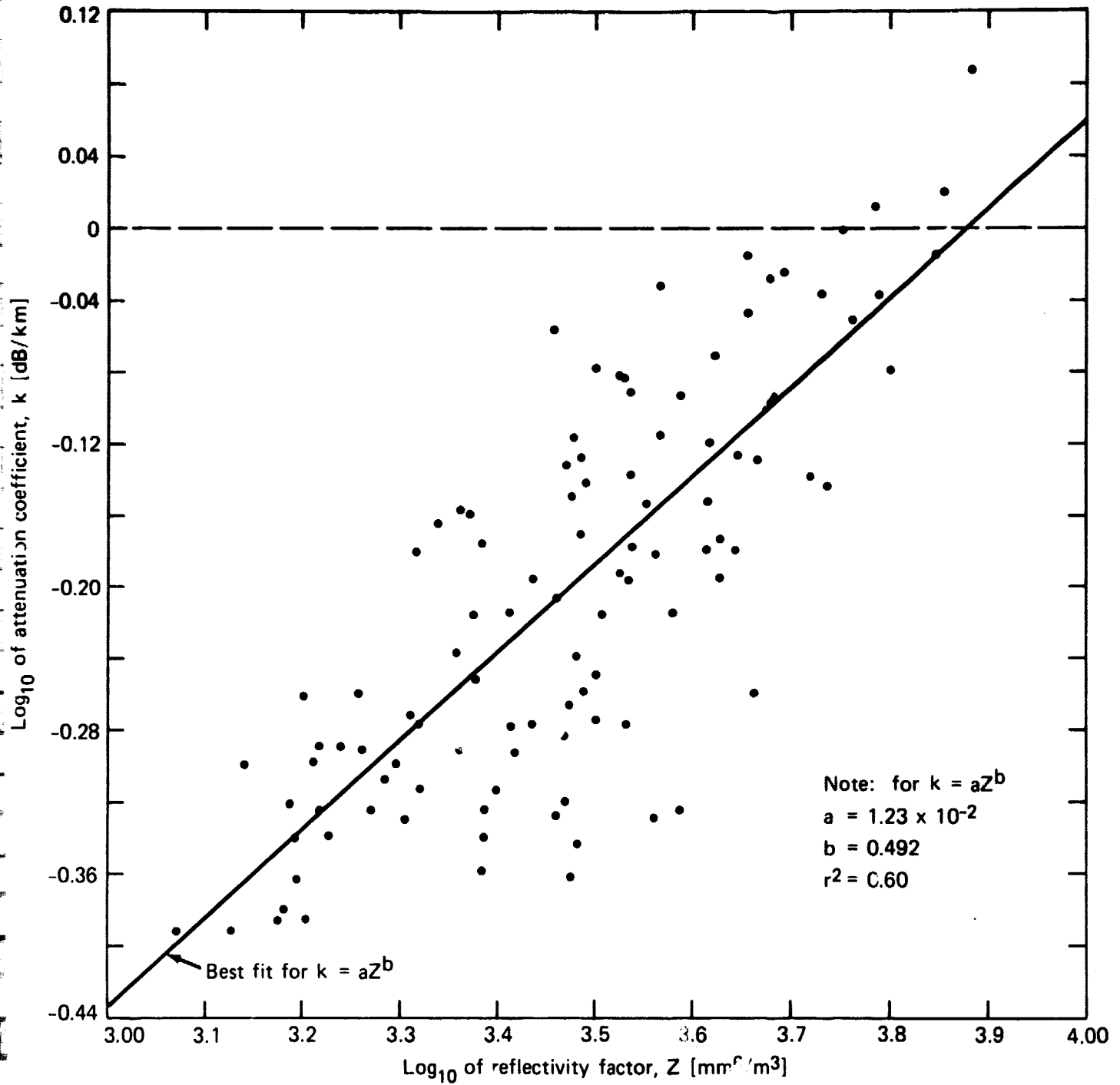
Figure 9. Scatter plot of log k vs log Z for early afternoon of
Aug 24, 1977 (day 236) from 14 hr, 21 min to 1ʒ hr, 30
min GMT. Solid line is best fit for k = a Z^b relation.
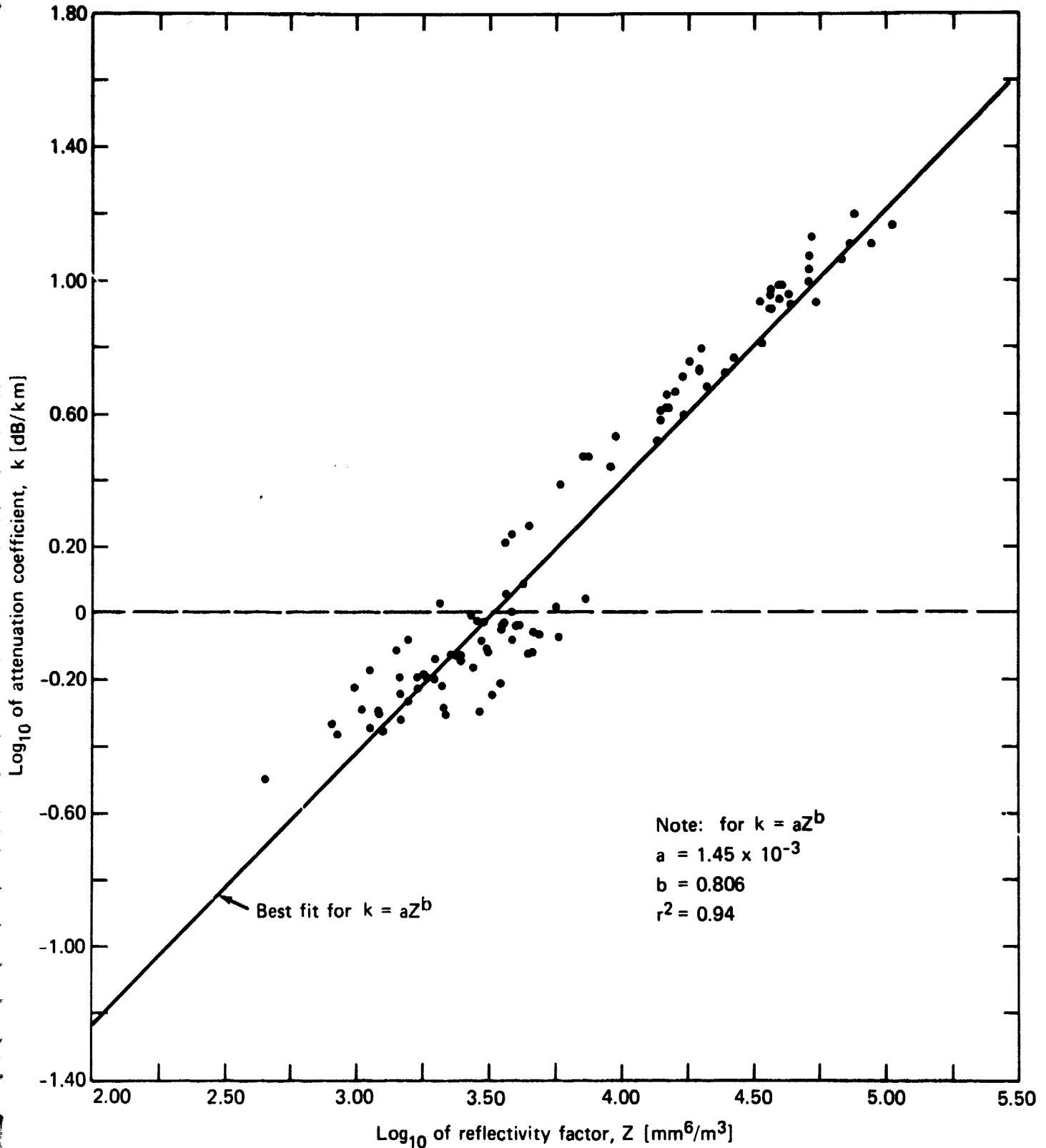
Figure 10. Scatter plot for log k vs log Z for evening of Aug 24 and morning of Aug 25, 1977 (days 236-237) from 23 hrs, 30 min to 00 hr, 52 min GMT. Solid line is best fit for $k = a Z^b$ relation.
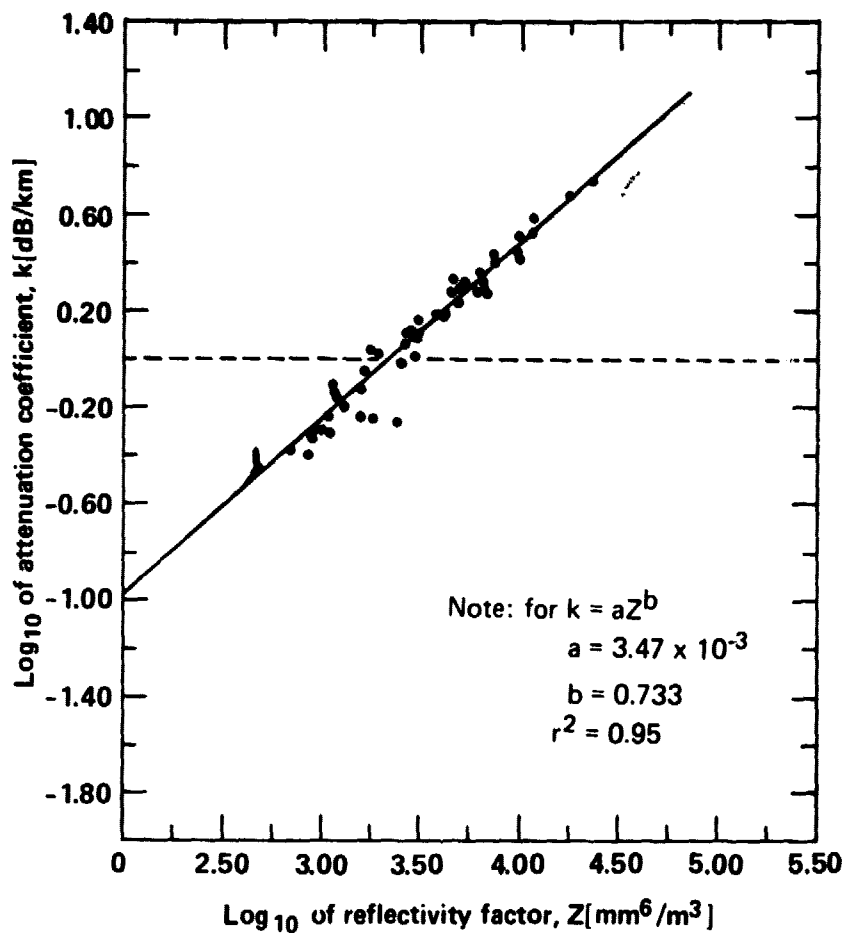
Figure 11. Scatter plot of log k vs log Z for Sept 14, 1977 (day 257) from 20 hr, 03 min to 20 hr, 46 min GMT. Solid line is best fit for k = a Z^b relation.
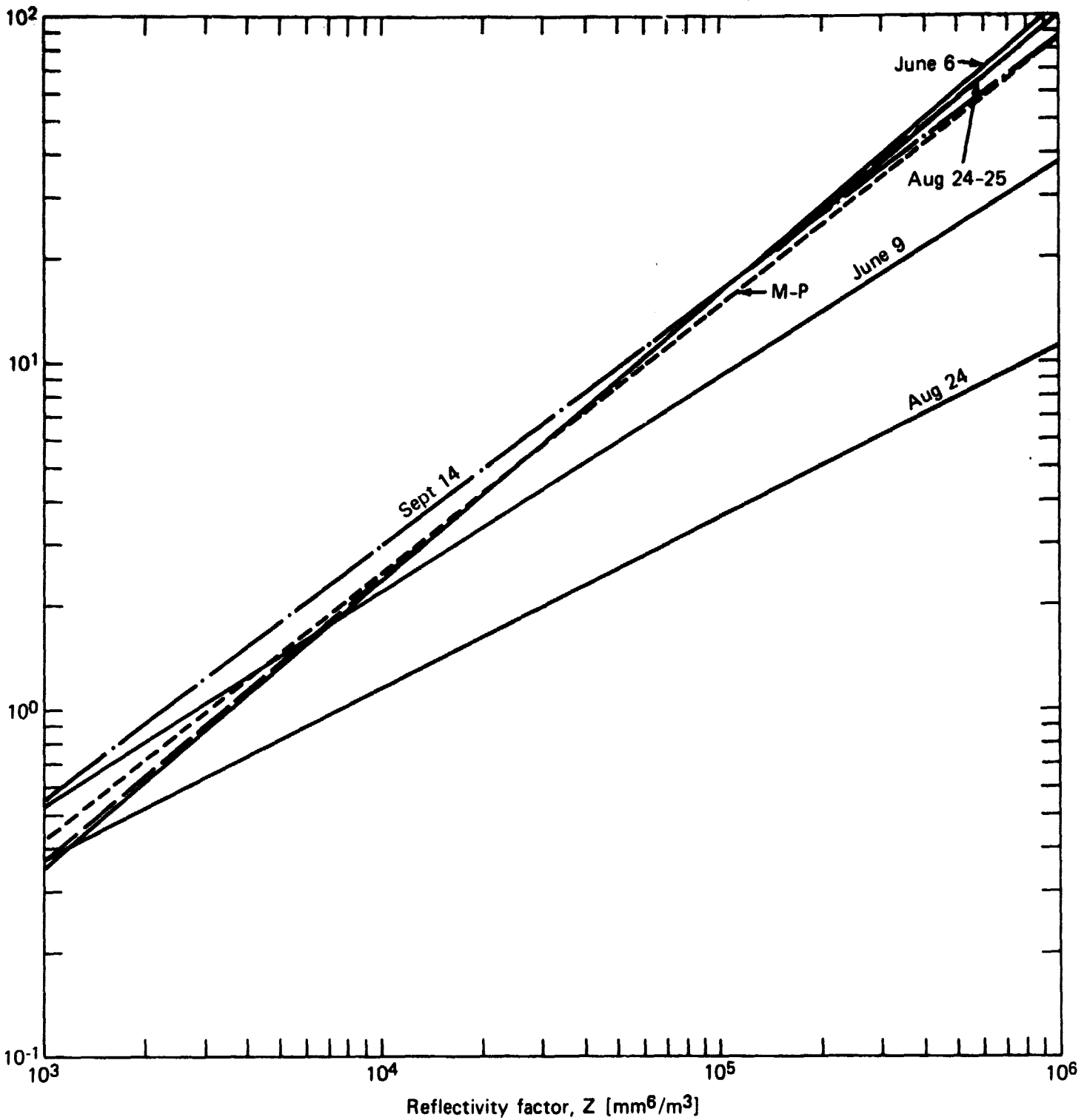
Figure 12. Comparison of best fit $k = a\, Z^{b}$ curves for five rain days with that of M-P.
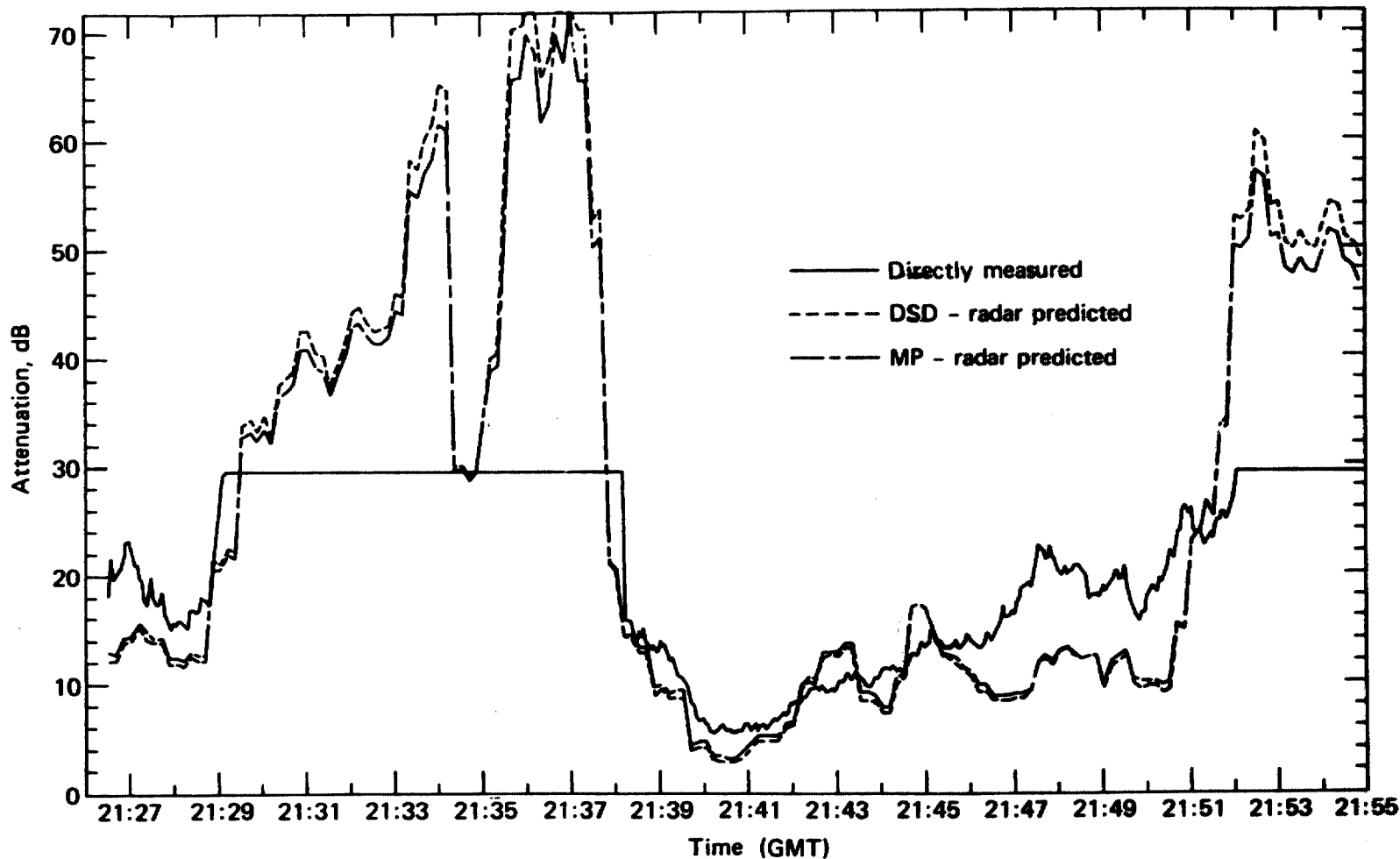
Figure 13. Comparison of directly measured fade event with DSD-radar predicted and
M-P-predicted for June 6, 1977 (day 157) from 21 hr, 26 min to 21 hr,
55 min GMT.
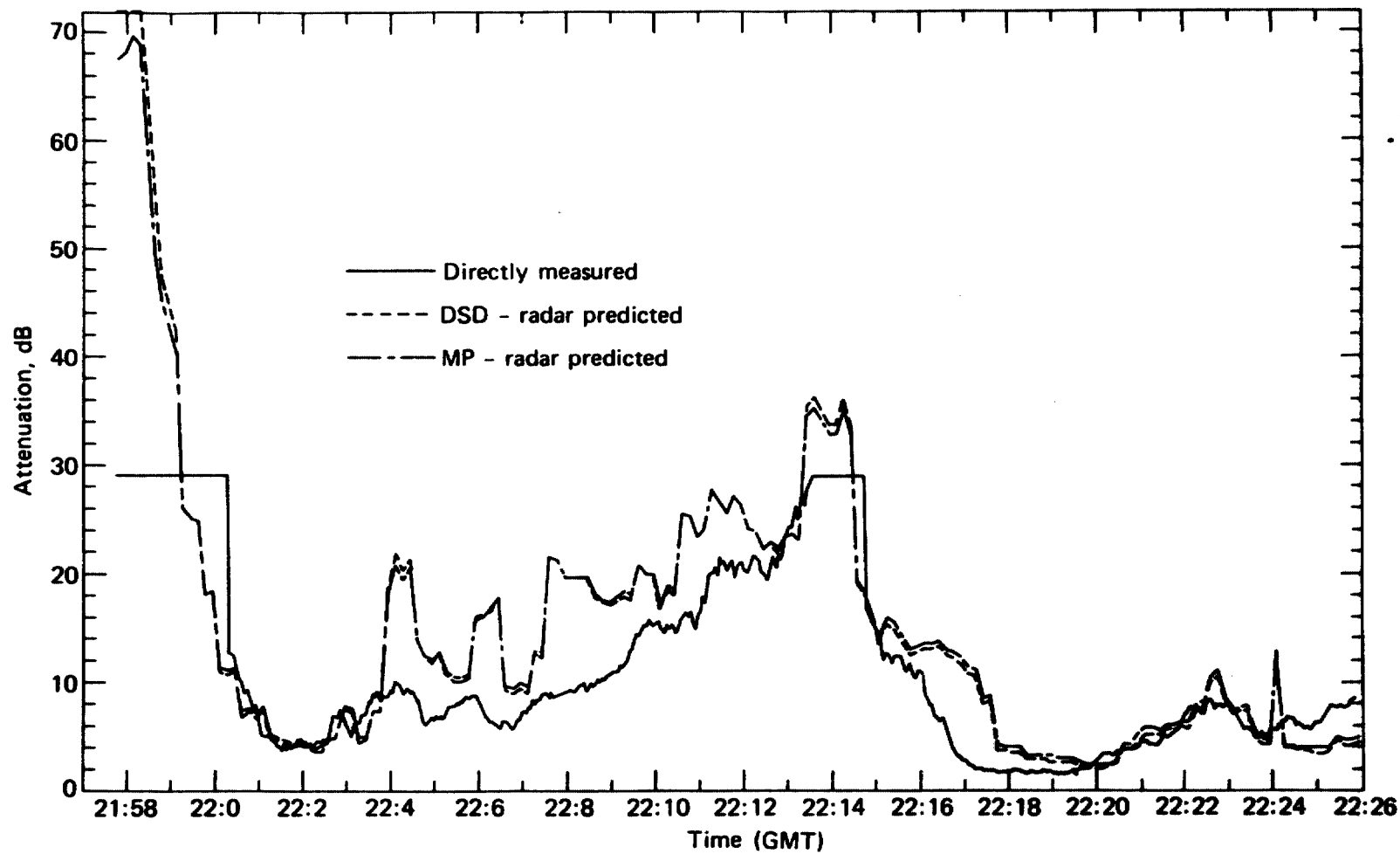
Figure 14. Comparison of directly measured fade event with DSD-radar predicted
and M-P-radar predicted for June 6, 1977 (day 157) from 21 hr, 57 min
to 22 hr, 25 min GMT.
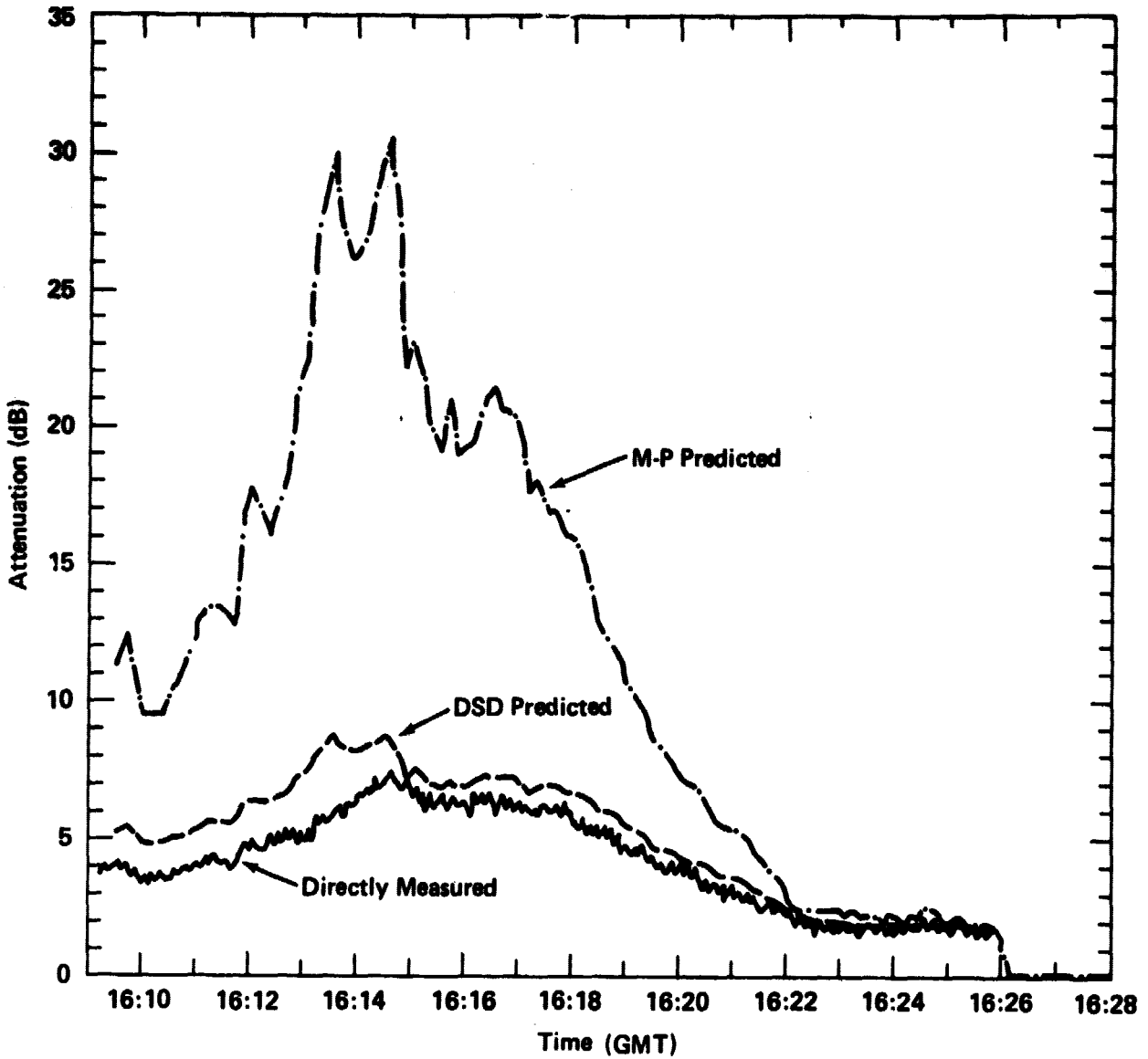
Figure 15. Comparison of directly measured fade event with DSD-radar predicted and M-P-radar predicted for early afternoon of Aug 24, 1977 (day 236) from 16 hr, 09 min to 16 hr, 26 min GMT.
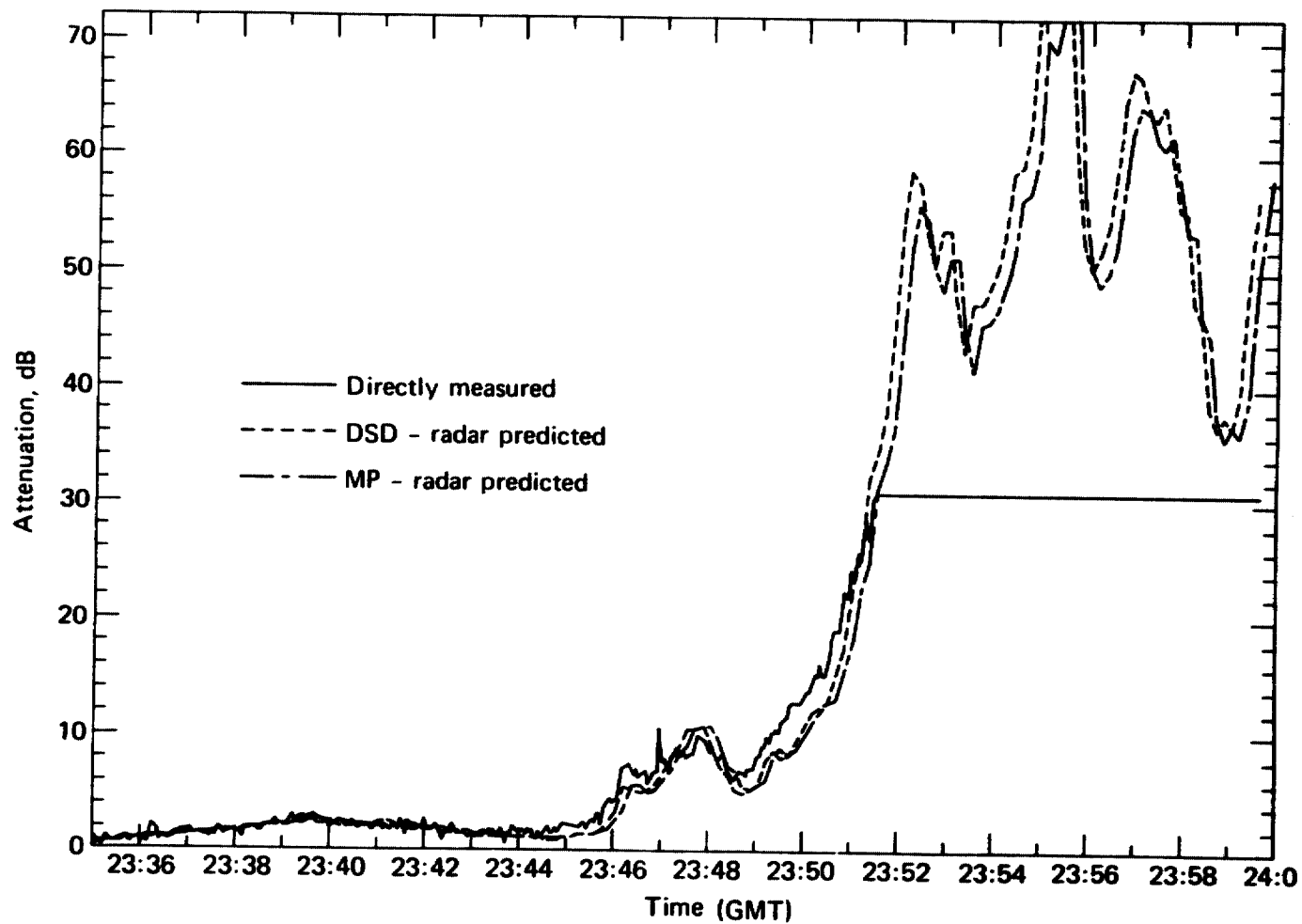
Figure 16. Comparison of directly measured fade event with DSD-radar predicted
and M-P-radar predicted for evening of Aug 24, 1977 (day 236) from
23 hr, 35 min to 23 hr, 59 min GMT.
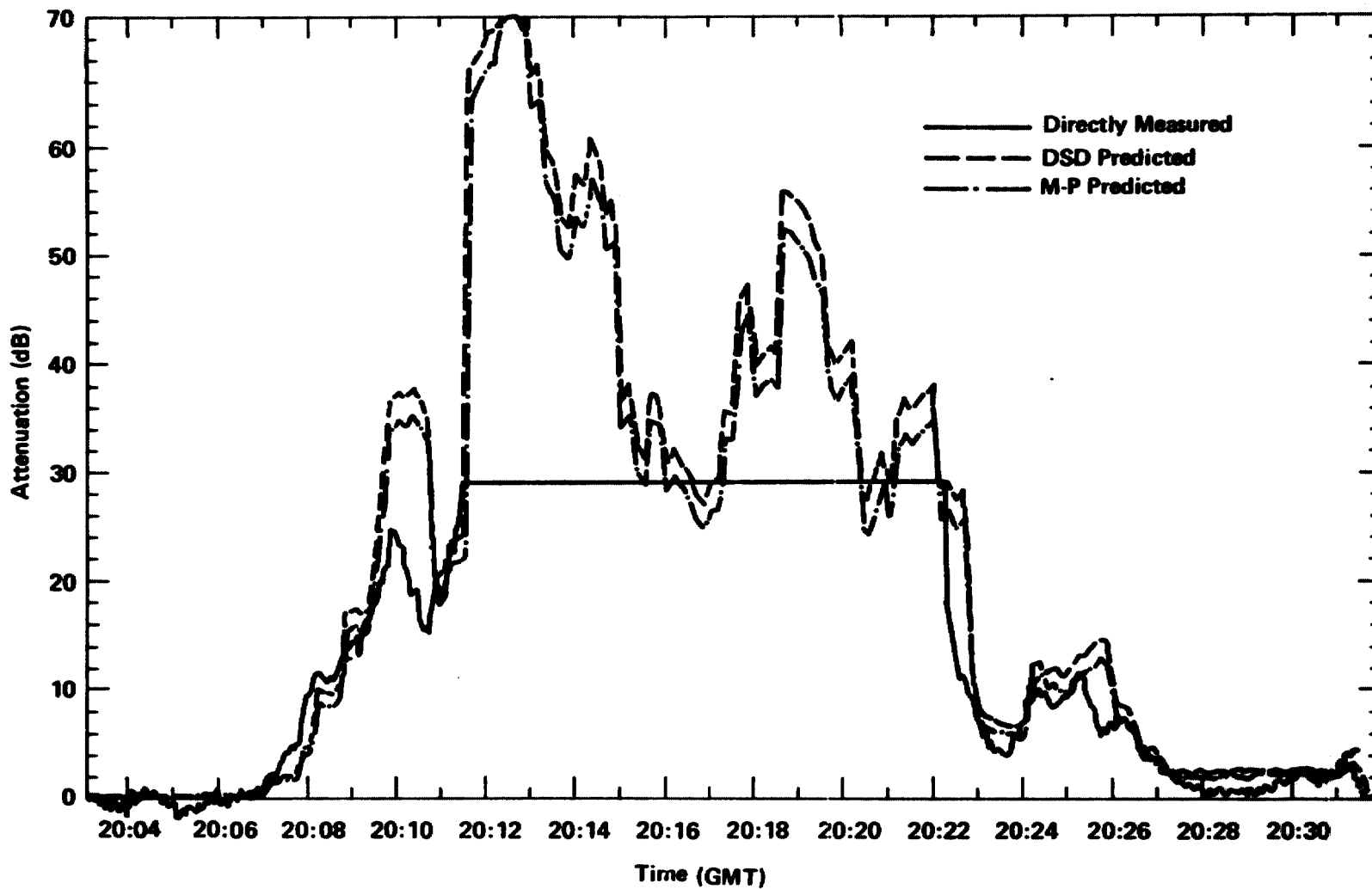
Figure 17. Comparison of directly measured fade event with DSD-radar predicted and M-P-radar predicted for Sept 14, 1977 (day 257) from 20 hr, 03 min to 20 hr, 32 min GMT.

curves are plotted from receiver data sampled at 3 second intervals and the
radar predicted curves are plotted from data samples at 10 second intervals.

The following interesting features may be noted from the above
comparisons: (1) The receiver dynamic range limits the maximum attenuation
excursion due to rain to approximately 30 dB beyond which a loss of lock
condition results. This accounts for the flattened sections of the curves.
The radar predicted levels do not suffer from this condition and show
attenuations sometimes in excess of 72 dB. (2) The directly measured and
predicted curves using DSD and radar measurements show overall good agree-
ment although slots of time do exist exhibiting large deviations. (3) On
those days in which the measured drop size spectra differed from M-P, the
radar predicted attenuation using the M-P distribution showed poor agreement
with the directly measured attenuation. An example of such case is depicted
in Fig. 15. On the other hand, the DSD predicted results show rather close
agreement. (4) For June 6 (Figs. 13 and 14), evening of August 24 (Fig. 16),
and September 14 (Fig. 17), the predicted attenuations using the measured
distributions are practically coincident with those of M-P. This, of course,
should be expected, as the measured values of a and b are similar to those
of M-P.

4.3 Measured and Predicted Probability Distributions

We here compare the cumulative fade distributions of the directly
measured and radar predicted cases. Such a comparison is given in Fig. 18.
The vertical scale represents the probability the attenuation exceeds the
abscissa; the abscissa corresponding to various attenuation levels. The
solid points, circles, and square points represent, respectively, the
directly measured, the DSD-radar predicted, and the M-P-radar predicted
distributions.

The table in Fig. 18 summarizes quantitatively how well the radar
predicted fade distributions agree with the measured ones. We note the rms
and average dB deviations for the radar-DSD case are 1.2 and 1.0 and the
average ratio of probabilities associated with the predicted and measured
points is 1.1. For the M-P case, the respective values are 5.6, 5.0, and 1.37.

Type	rms dB deviation	Avg dB deviation	Avg prob. ratio
DSD	1.2	1.0	1.09
M-P	5.6	5.0	1.37

● Directly measured
○ Disdrometer predicted
◻ M-P predicted
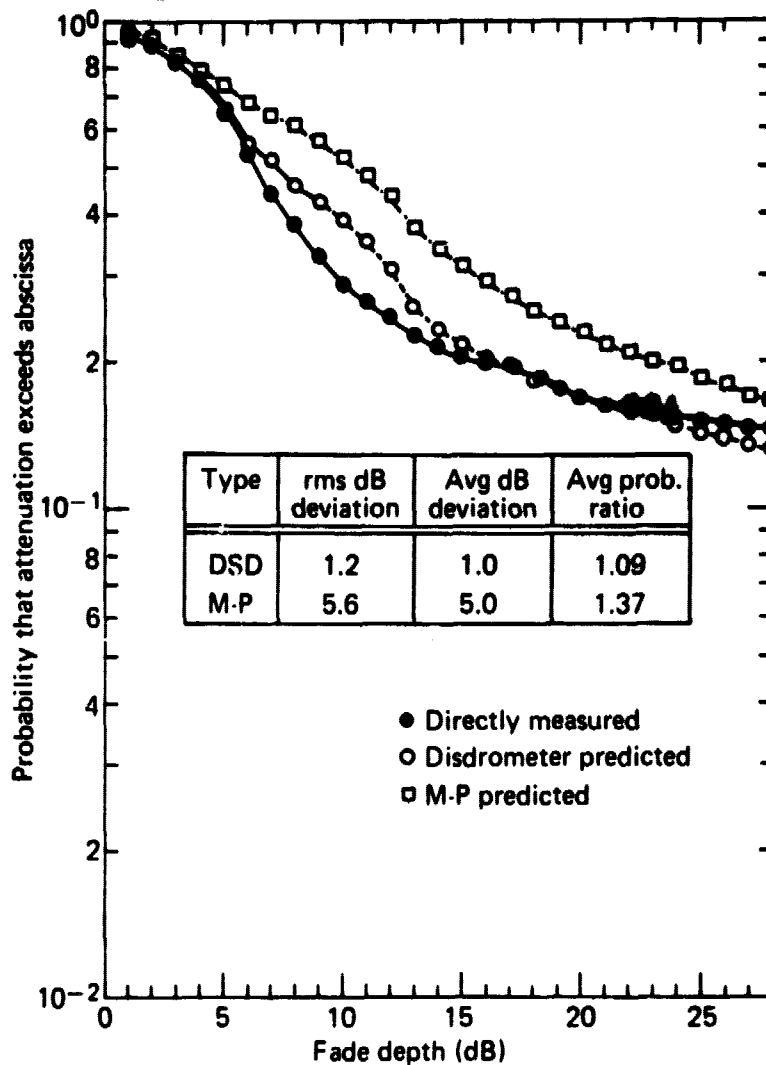
Figure 18. Comparison of cumulative distributions for directly measured, DSD-radar predicted, and M-P-radar predicted cases covering five rain days, 304 minutes of simultaneous radar sampling during summer of 1977.

The average probability ratio of the two curves was obtained by averaging the ratio of the larger probability to the smaller one for each dB level up to 28 dB. This gives a measure of the percentage uncertainty of the predicted curve relative to the measured one. Hence, on an absolute basis, the disdrometer curve shows very good agreement with the directly measured whereas the M-P curve shows poorer agreement. Whether this would tend to obviate the use of the M-P spectra for such radar predictions is too early to say, as an increased data base might bring the M-P radar predicted distribution in closer agreement with the directly measured one.

4.4 Empirical Calibration Adjustment

An adjustment in the radar calibration was deemed necessary in arriving at the reflectivity factors, Z; otherwise, the radar predicted attenuation levels consistently underestimate the directly measured values. When the reflectivity values were increased by multiplying by an empirically determined fixed factor of 3.5 (5.4 dB), both the case-by-case attenuation events as well as the cumulative distribution showed good agreement. The reason for this required adjustment is not at present understood although it might in part be due to a phenomenon described by Rogers [14]. Rogers demonstrated that for the case in which the backscatter is measured through a logarithmic receiver and there are simultaneously large gradients of reflectivity in the radar pulse volume, estimated reflectivity levels deviate from the true averages by an amount depending upon the gradient value of Z in the pulse volume. For example, according to one model, if there is a logarithmic variation of Z in the pulse volume with a ratio of maximum to minimum Z of 6, this could account for a 6 dB underestimation of the reflectivity factor.

Another possible reason for underestimations of the peak attenuation values may be due to the comparative spatial resolutions of the receiving and radar systems. The attenuation of the received beacon signal takes place essentially through the first Fresnel spheroidal region whose diameter is given by

$$D(FZ) = 2(r_0 \lambda)^{1/2} = 0.205 \; r_0^{1/2} \qquad [m]$$

where r_o [m] is the axial distance from the receiving antenna and λ [m] is the beacon wavelength. The diameter of the cross section of the radar beamwidth ($\theta = 0.4°$) is given by,

$$D_R = 6.98 \times 10^{-3} \, r_o \qquad [m]$$

and the ratio of these diameters is,

$$\frac{D_R}{D(FZ)} = 3.4 \times 10^{-2} \, r_o^{1/2} \qquad [m]$$

We note that at a distance of 6 km the diameter associated with the radar beamwidth is approximately 2.5 times the Fresnel zone diameter and at 1 km they are equivalent. The received beacon signal is therefore expected to have greater attenuation peaks than that estimated by the radar because of the differences in averaging that takes place across the beams.

5.0 SUMMARY, DISCUSSION, AND CONCLUSIONS

Although the overall data base was limited, the DSD and radar results showed the following salient features:

(1) The radar predicted attenuations using the measured rain drop spectra showed generally good agreement on a case by case basis with the directly measured levels; although slots of time exist exhibiting deviations. On the other hand, extended rain periods exist where the M-P radar predicted curves show overall poor agreement.

(2) The DSD-radar predicted cumulative fade distributions show very good agreement with the directly measured ones whereas the M-P results showed poorer agreement.

(3) When the coefficient of correlation was high (i.e., $r^2 > 0.9$), the measured disdrometer results were in close agreement with the M-P spectra; and conversely.

Two distinct advantages of using radar results appear in the curves shown in Figs. 13, 14, 16, and 17. First, no limitation for examining severe

attenuation levels exists in the radar predicted cases as does exist in a fixed dynamic range receiver. Secondly, the receiver used could not reacquire lock until it was 7 to 8 dB below the loss of lock condition and this reacquisition might take place only after a frequency search which could take several minutes. The radar measurements do not suffer from these intrinsic receiver characteristics. On the other hand, the radar predicted measurements do suffer from other features and these are: (1) An absolute calibration of the radar is necessary, (2) The drop size distribution may be both spatially and temporally variable, (3) The attenuation for the received satellite signal occurs along a narrow Fresnel ellipsoid whose maximum cross section diameter is 20 m whereas the radar prediction measures the average reflectivity of the radar beamwidth which may have approximately 3 times the cross section diameter, (4) The radar reflectivities are averaged over a pulse volume defined by the antenna beamwidth and the range resolution interval of 150 m within which the reflectivities may be highly non-uniform, (5) The beam axis of the radar and the receiver system are not coincident; being displaced by 30 m, (6) Near field correction formulations applied to the radar antenna system are based on idealized assumptions, and (7) The pulse volumes may contain snow or ice near the zero degree isotherm height.

In spite of the many reasons for non-correlation, the radar results do correlate remarkable well for the above example. In fact, the above results demonstrate the utility of using radar coupled with disdrometers measurements for predicting individual fade events as well as long term fade distributions associated with satellite communications through rain. It also suggests its use for arriving at sampled fade distributions from which prediction criteria associated with variable frequencies, path angles, and site diversity can be tested [15].

In the absence of DSD spectra, the M-P distribution might represent a viable alternative for use with the radar measurements; at least for the mid-Atlantic coast geographic region. An insufficient data base, however, exists here to be definitive about this assessment.

6.0 ACKNOWLEDGEMENTS

7.0 REFERENCES

1. McCormick, K. S., "A Comparison of Precipitation Attenuation and Radar Backscatter along Earth-Satellite Paths", IEEE Trans. on Antennas and Propagation, Vol. AP-20, No. 6, pp 747-755, Nov 1972.

2. Strickland, J. I., "Radar Measurements of Site Diversity Improvement During Precipitation", Journal Des Researches Atmospheriques, Colloque De L'IUCRM, Vol. VIII, pp 451-464, January-June 1974.

3. Goldhirsh, J., "Attenuation of Propagation Through Rain for an Earth-Satellite Path Correlated with Predicted Values Using Radar", IEEE Trans. on Antennas and Propagation, Vol. AP-23, No. 6, pp 786-791, Nov. 1975.

4. Hodge, D. B. and G. L. Austin, "The Comparison Between Radar- and Radiometer-Derived Rain Attenuation for Earth-Space Links", Radio Science, Vol. 12, No. 5, pp 733-740, Sept-Oct 1977.

5. Marshall, J. S. and W. McK. Palmer, "The Distribution of Raindrops With Size", J. Meteor., Vol. 5, pp 165-166, Aug 1948.

6. Katz, I., A. Arnold, J. Goldhirsh, T. G. Konrad, W. L. Vann, E. B. Dobson, and J. R. Rowland, "Radar Derived Spatial Statistics of Summer Rain - Experiment Description", NASA Contractor Report No. NASA CR-2592, Vol. I of III, prepared by Applied Physics Laboratory, The Johns Hopkins University, Johns Hopkins Road, Laurel, Maryland 20810 for Goddard Space Flight Center, Greenbelt, Maryland 20771, Sept 1975.

7. Goldhirsh, J., "Measured Radar Parameters and Error Budget Associated with SPANDAR and the CLC Program", APL Technical Report MPD73U-054, July 1973.

8. Goldhirsh, J. and J. C. Howard, "Results of Sphere Calibration of SPANDAR and Comparison with Other Measurements", APL Technical Report F1E74U-040, Nov 1974.

9. Goldhirsh, J., "Measurement of Antenna Gain Using the Sun as a Radio Source", APL Technical Report F1E76U-006, March 1976.

10. Rowland, J. R., "Comparison of Two Different Raindrop Disdrometers",
    Proc. 17th Conf. on Radar Meteor., Seattle, Wash., pp 398-405, Oct.
    26-29, 1976 (American Meteorological Society, 45 Beacon St., Boston,
    Mass. 02108).

11. Rowland, J. R., L. W. Bennett, and R. E. Miller, "Description of the
    APL Disdrometer-Raingage System", APL Technical Report F1E75U-026,
    Sept 1976.

12. Hansen, R. C., "Microwave Scanning Antennas, Vol. 1 - Apertures",
    Academic Press, New York, 1964.

13. Medhurst, R. G., "Rain Attenuation of Centimeter Waves: Comparison
    of Theory and Measurement", IEEE Trans. on Antennas and Propagation,
    Vol. AP-13, pp 550-564, July 1975.

14. Rogers, R. R., "The Effect of Variable Targer Reflectivity on Weather
    Radar Measurements", Quart. J. Roy. Meteor. Soc., Vol. 97, pp 154-167,
    1971.

15. Goldhirsh, J., "Prediction Methods for Rain Attenuation Statistics
    at Variable Path Angles and Carrier Frequencies Between 13 and 100
    GHz", IEEE Trans. on Antennas and Propagation, Vol. AP-23, No. 6,
    Nov 1975.

Appendix A

DERIVATIONS OF THE RADAR EQUATION IN THE NEAR FIELD OF SPANDAR

The antenna of SPANDAR may be approximated by a circular aperture with a tapered illumination having the cross section distribution given by $[1-(\frac{\rho}{D/2})^2]$ where ρ is the cross section radial distance and $D/2$ is the radius. Using the results of Hansen [12] the gain, $G(r)$, and beamwidth, $\theta(r)$, in the near region of this aperture (i.e., $r \le 2 D^2/\lambda$) are range dependent and are given by,

$$\theta(r) = \theta_o \, \gamma(r) \tag{A.1}$$

$$G(r) = \frac{G_o}{\gamma^2} \tag{A.2}$$

where

$$\gamma(r) = \frac{\pi}{16X}\left\{1 - \frac{16X}{\pi} \, Sin\left(\frac{\pi}{8X}\right) + \frac{128X^2}{\pi^2}\left[1 - Cos\left(\frac{\pi}{8X}\right)\right]\right\}^{-1/2} \tag{A.3}$$

where

$$X = \frac{r}{r_f} \; ; \; r_f = \frac{2D^2}{\lambda} \tag{A.4}$$

and where G_o and θ_o are the far field gain and beamwidth, respectively.

We assume that the radar equation in the near region to have the same form as that in the far region with the exception that the beamwidths and gains are range dependent. That is,

$$P_r = \left(\frac{c}{1024 \, \pi^2 \, \ell n \, 2}\right)\left(P_t \, \tau \, \lambda^2 \, \eta\right)\frac{G^2(r) \, \theta_e(r) \, \theta_h(r)}{2} \tag{A.5}$$

where

c = the velocity of light (m/sec)

P_t = the transmitted power (watts)

τ = the pulse width (sec)

η = the reflectivity (m^{-1})

λ = the wavelength (m)

r = the range (m)

Dividing (A.5) by the far field formulation, we obtain

$$\frac{P_r}{P_{ro}} = \frac{G^2(r)\ \theta_e(r)\ \theta_h(r)}{G_o^2\ \theta_{eo}\ \theta_{ho}} \tag{A.6}$$

where the subscript o denotes the far field values.

Substituting (A.1) and (A.2) into (A.6)

$$\frac{P_r}{P_{ro}} = \frac{1}{\gamma^2(r)} = \frac{G(r)}{G_o} = \left(\frac{r}{r_f}\right)^2 \beta(r) \tag{A.7}$$

where from (A.3), $\beta(r)$ is given by,

$$\beta(r) = \frac{256}{\pi^2}\left\{1 - \frac{16X}{\pi}\ \mathrm{Sin}\left(\frac{\pi}{8X}\right) + \frac{128X^2}{\pi^2}\left[1 - \mathrm{Cos}\left(\frac{\pi}{8X}\right)\right]\right\} \tag{A.8}$$

We note from (A.7) that the far zone power formulation, P_{ro}, is modified by a correction factor equal to the ratio of the near to the far field gains. In Fig. 7, 10 Log_{10} of $\gamma^2(r)$ is plotted down to 600 m from SPANDAR. We note that this parameter monotonically increases down to this range reaching a value of 4.3 dB. The far zone power formulation must therefore be reduced by the indicated levels in the near zone region.